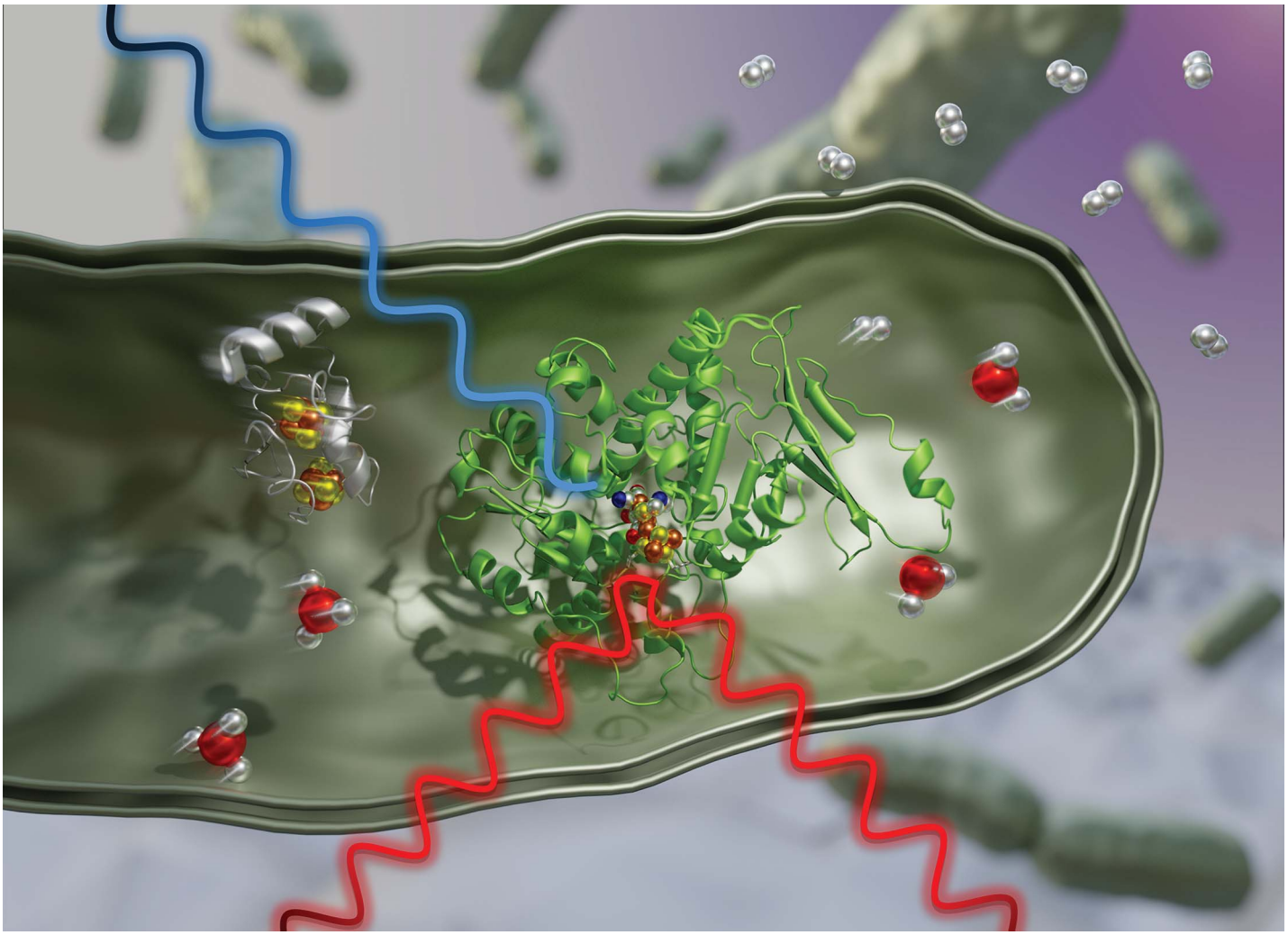

Showcasing research from the laboratories of Professor Berggren, Department of Chemistry, Uppsala University, Sweden; and Dr. Stripp, Department of Physics, Freie Universität Berlin, Germany.

Spectroscopic investigations under whole-cell conditions provide new insight into the metal hydride chemistry of [FeFe]-hydrogenase

[FeFe]-hydrogenases are gas processing enzymes that catalyse H^+/H_2 interconversion with remarkable efficiency, making them highly relevant in a biotechnological context. Their chemistry is enabled by an organometallic cofactor, the "H-cluster". In this study, the biologically unique H-cluster is studied under whole-cell conditions, using electron paramagnetic resonance and infrared difference spectroscopy. For the first time, a number of proposed catalytic intermediates are observed in living cells, supporting their physiological relevance. This includes two reactive metal hydride species, considered to be key intermediates in the final stages of H_2 formation. Cover art prepared by Dr Emanuel Pfitzner.

As featured in:

See Sven T. Stripp, Gustav Berggren *et al.*, *Chem. Sci.*, 2020, **11**, 4608.

ROYAL SOCIETY OF CHEMISTRY

rsc.li/chemical-science

Registered charity number: 207890

Chemical Science

ROYAL SOCIETY OF CHEMISTRY

EDGE ARTICLE

View Article Online
View Journal | View Issue

Cite this: *Chem. Sci.*, 2020, **11**, 4608

All publication charges for this article have been paid for by the Royal Society of Chemistry

Spectroscopic investigations under whole-cell conditions provide new insight into the metal hydride chemistry of [FeFe]-hydrogenase†

Lívia S. Mészáros, ‡[a] Pierre Ceccaldi, ‡[a] Marco Lorenzi, [a] Holly J. Redman,[a] Emanuel Pfitzner, [b] Joachim Heberle, [b] Moritz Senger, [b] Sven T. Stripp *[b] and Gustav Berggren *[a]

Hydrogenases are among the fastest H_2 evolving catalysts known to date and have been extensively studied under *in vitro* conditions. Here, we report the first mechanistic investigation of an [FeFe]-hydrogenase under whole-cell conditions. Functional [FeFe]-hydrogenase from the green alga *Chlamydomonas reinhardtii* is generated in genetically modified *Escherichia coli* cells by addition of a synthetic cofactor to the growth medium. The assembly and reactivity of the resulting semi-synthetic enzyme was monitored using whole-cell electron paramagnetic resonance and Fourier-transform Infrared difference spectroscopy as well as scattering scanning near-field optical microscopy. Through a combination of gas treatments, pH titrations, and isotope editing we were able to corroborate the formation of a number of proposed catalytic intermediates in living cells, supporting their physiological relevance. Moreover, a previously incompletely characterized catalytic intermediate is reported herein, attributed to the formation of a protonated metal hydride species.

Received 28th January 2020
Accepted 14th April 2020

DOI: 10.1039/d0sc00512f

rsc.li/chemical-science

Introduction

Hydrogenases are gas processing metalloenzymes that interconvert protons (H^+) and molecular hydrogen (H_2) with remarkable efficiency. The so-called [FeFe]-hydrogenases are considered the most efficient H_2 producers in nature, with reported turnover frequencies up to 10 000 H_2 per second.[1,2] This reactivity makes [FeFe]-hydrogenases highly relevant for biotechnological H_2 production as an alternative to platinum-based electrolysis[3–6] and a biological blue-print for the design of synthetic catalysts.[7–9] Consequently, intense efforts have been invested in elucidating the structure and catalytic mechanism of these enzymes.[10,11]

The reactivity of [FeFe]-hydrogenases is enabled by a hexanuclear iron complex, referred to as the hydrogen-forming cluster or simply the "H-cluster" (Fig. 1). This cofactor consists of a canonical iron–sulfur cluster ($[4Fe\text{–}4S]_H$) coupled to an organometallic diiron subsite ($[2Fe]_H$). The low-valent iron ions of the $[2Fe]_H$ subsite are bridged by an azadithiolate ligand ($^-SCH_2NHCH_2S^-$, adt) and further coordinated by strong-field ligands like carbon monoxide (CO) and cyanide (CN^-).[12–15]

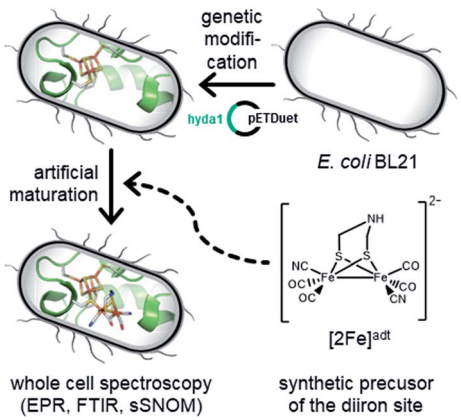

Fig. 1 Schematic representation of the whole-cell assembly and spectroscopic investigation of the resulting semi-synthetic H-cluster. Genetic modification of *E. coli* for expression of [FeFe]-hydrogenase apo-protein, followed by synthetic maturation generates functional hydrogenase (the H-cluster is shown in the H_{ox} state). The reactivity of this semi-synthetic enzyme is probed in whole cells by EPR and ATR FTIR spectroscopy. Proposed key intermediates were observed in cells for the first time, and conditions for accumulating a protonated hydride state (denoted $H_{hyd}H^+$) are reported. In parallel, the integrity of the cells is verified by AFM imaging and near-field IR spectroscopy.

[a]*Molecular Biomimetics, Dept. of Chemistry – Ångström Laboratory, Uppsala University, Lägerhyddsvägen 1, SE-75120, Uppsala, Sweden. E-mail: gustav.berggren@kemi.uu.se*

[b]*Institute of Experimental Physics, Experimental Molecular Biophysics, Freie Universität Berlin, Arnimallee 14, Berlin, DE-14195, Germany. E-mail: sven.stripp@fu-berlin.de*

† Electronic supplementary information (ESI) available: Including additional EPR and FTIR data, AFM images of *E. coli* cells, cell viability data, *in vitro* enzymatic assay data, as well as an overview of the sSNOM and nanoFTIR setup. See DOI: 10.1039/d0sc00512f

‡ These authors contributed equally.

Due to its unique nature, the biosynthesis of the $[2Fe]_H$ subsite requires at least three hydrogenase specific maturation enzymes.[16–20] Despite challenges in preparing the enzyme, extensive *in vitro* work has revealed a number of potential catalytic intermediates (Scheme 1). The oxidized resting state of the enzyme (H_{ox}) exhibits a mixed-valence $[2Fe]_H$ subsite and an oxidized $[4Fe–4S]_H$ cluster ($[4Fe–4S]_H^{2+}$-$[Fe(I)Fe(II)]_H$).[21,22] Under acidic conditions $H_{ox}H$ is formed, attributed to a protonation at the $[4Fe–4S]_H$ cluster.[23,24] Reduction of H_{ox} by one electron results in either H_{red}' or H_{red} (the latter also referred to as "$H_{red}H^+$").[23,25,26] The H-cluster shows a reduced and possibly protonated $[4Fe–4S]_H$ cluster in H_{red}' whereas in H_{red} the $[2Fe]_H$ site is reduced and protonated.[27] Further reduction of H_{red} generates the "super-reduced" state, H_{sred}, identified as a $[4Fe–4S]_H^+$-$[Fe(I)Fe(I)]_H$ species.[28]

The exact nature of these intermediate states and their relevance to the catalytic mechanism is under debate.[10,27,30–33] However, all recent models agree that a terminal hydride is formed during catalysis. One such intermediate, denoted H_{hyd}, has been detected *in vitro* and shown to accumulate in amino acid variants with disrupted proton transfer networks, but also in the native enzyme under reducing conditions at low pH.[29,34–39] The H_{hyd} state features a terminal hydride on the $[2Fe]_H$ subsite (Scheme 1) and the electronic structure of this state comprises a diamagnetic $[Fe(II)Fe(II)]_H$ subsite coupled to a paramagnetic $[4Fe–4S]_H^+$ cluster.[29,35] Protonation of this latter species, presumably on the nitrogen bridgehead of the adt ligand, is expected to form the so-called $H_{hyd}H^+$ state, as a potentially final metastable intermediate prior to H–H bond formation and H_2 release. However, this latter state is still incompletely characterized and its electronic and geometric structure remains to be clarified.[29,40]

The biological maturation machinery required for H-cluster assembly can be circumvented by incubating [FeFe]-hydrogenase apo-protein with synthetic mimics of the $[2Fe]_H$ subsite. Under *in vitro* conditions it is well established that the incorporation of the $[Fe_2(adt)(CO)_4(CN)_2]^{2-}$ complex ($[2Fe]^{adt}$) results in the spontaneous assembly of semi-synthetic hydrogenases indistinguishable from the native enzyme ($[2Fe]^{adt}$-HydA1).[7,13,41–43] We recently adopted this strategy for *in vivo* applications, enabling the preparation of fully functional, semi-synthetic enzymes in both *E. coli* and cyanobacteria.[6,44–46] Herein, we take advantage of this protocol to perform spectroscopic investigations of [FeFe]-hydrogenase in whole cells (Fig. 1). This approach provides new mechanistic insight as it allows us to probe the formation of proposed key intermediates under relatively mild conditions more similar to the native environment of the enzyme.

We combine whole-cell electron paramagnetic resonance (EPR) and Fourier-transform infrared (FTIR) spectroscopy to characterize the enzymatic activity and catalytic mechanism of an [FeFe]-hydrogenase from the photosynthetic green alga *Chlamydomonas reinhardtii*, HydA1.[47] In parallel, individual cells were characterized by atomic force microscopy (AFM), scattering-type scanning near-field optical microscopy (sSNOM) and nano-FTIR spectroscopy, verifying cellular integrity and protein content. Through a combination of gas flushes and pH changes we detected a number of proposed catalytic intermediates, including H_{ox}, $H_{ox}H$, and H_{red}, supporting their catalytic relevance. The present study also provides the first demonstration of the formation of reactive metal hydride species in living cells, as the H_{hyd} state accumulates in whole cells under reducing conditions mimicking the native environment of the enzyme, *i.e.* the weakly alkaline stroma of the chloroplast in *C. reinhardtii*. Moreover, the formation of a protonated hydride state is observed under mildly acidic and strongly reducing conditions.

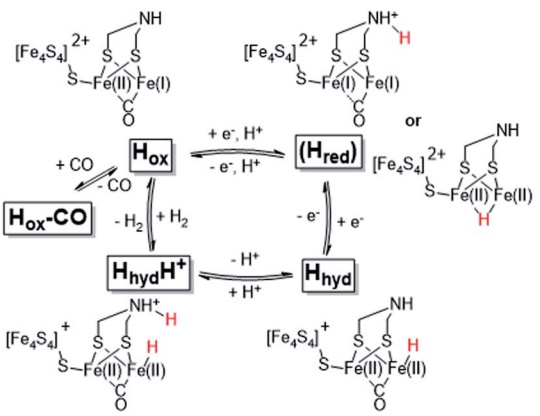

Scheme 1 Schematic representation of the catalytic cycle of [FeFe]-hydrogenase, based on the states observed under whole-cell conditions including the protonated hydride species ($H_{hyd}H^+$). The catalytic cycle is derived from ref. 10 and 29, and the debated H_{red} state is shown in parenthesis together with two proposed structures (protonated on the ligand or metal, respectively).

Results and discussion

In vivo assembly of the semi-synthetic H-cluster

To generate active hydrogenase in concentrations suitable for whole-cell spectroscopy, the HydA1 protein was heterologously expressed in BL21(DE3) *E. coli* cells, similar to previous reports.[44–46] The absence of the [FeFe]-hydrogenase specific maturation machinery in *E. coli* results in the synthesis of an inactive form of the enzyme containing the $[4Fe–4S]_H$ cluster but lacking the $[2Fe]_H$ subsite (apo-HydA1). 50 mL cell cultures were concentrated to 2 mL and depleted of O_2 at which point the synthetic cofactor mimic $[2Fe]^{adt}$ was added to the medium, and the H-cluster assembly monitored by EPR spectroscopy and H_2 production assays. The apo-enzyme remained undetected in our experiments, due to the intensity of underlying signals attributed to other iron–sulfur proteins in *E. coli* (Fig. 2A and S1†). Conversely, the formation of the H-cluster was readily observable by whole-cell EPR spectroscopy (Fig. 2A). Incubation of the cell suspensions for 1 h in the presence of low concentrations (0.008–0.8 μM) of the synthetic $[2Fe]^{adt}$ cofactor resulted in the appearance of a rhombic EPR signal attributable to H_{ox} (g = 2.100; 2.040; 1.998).[48] This rhombic signal was clearly discernable in spectra, but of small intensity relative to the background signal from the cells (Fig. 2A compare the black spectrum, "control", to blue and green, 0.08 μM–0.8 μM, spectra, see also Fig. S1† for non-background subtracted spectra and

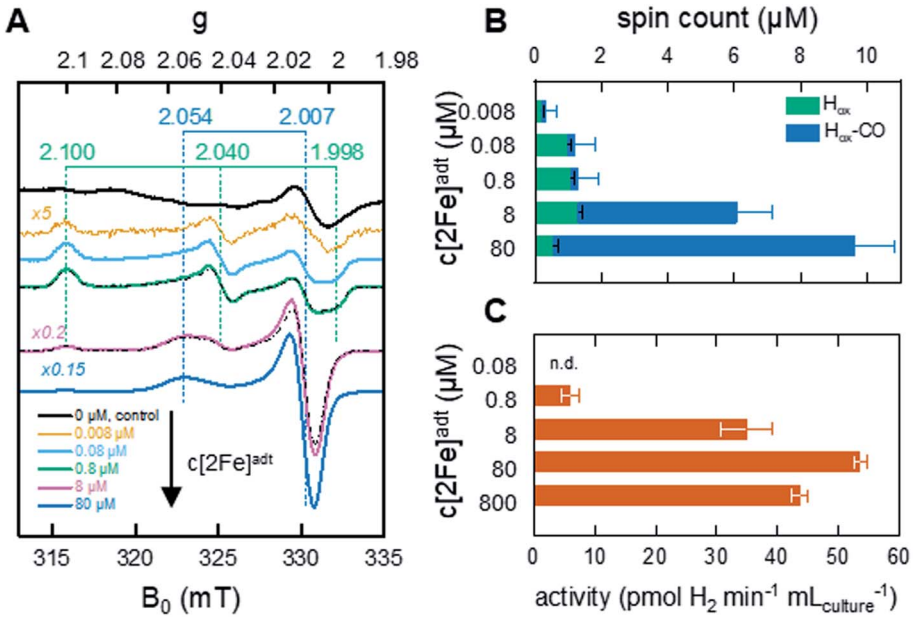

Fig. 2 *In vivo* H-cluster assembly monitored by EPR spectroscopy and H_2 gas production. (A) Whole-cell EPR spectra of apo-HydA1 (control, 0 μM $[2Fe]^{adt}$ added) and $[2Fe]^{adt}$-HydA1 containing cell suspensions, concentrated to 400 μL. H-cluster assembly occurs spontaneously upon addition of $[2Fe]^{adt}$ to the medium, with H_{ox} being the favored state at low $[2Fe]^{adt}$ concentrations. As the concentration of the synthetic cofactor increases, the cell samples become dominated by the H_{ox}–CO state. The *g*-values of H_{ox} (green dashed lines) and H_{ox}–CO (blue dashed lines) states are based on simulations of the two samples at 0.8 and 8 μM (black dash-dotted lines). All $[2Fe]^{adt}$-HydA1 spectra were corrected for contribution from the cells by subtracting the signal of the apo-HydA1 control sample (black spectrum). EPR experimental conditions: $T = 20$ K, $P = 1$ mW, $\nu = 9.28$ GHz. (B) Concentrations of the H_{ox} (green bars) and H_{ox}–CO (blue bars) signals in each sample, extrapolated from the simulations. The full length of the bar reflects total spin count. Error bars indicate estimated relative error from simulations, in addition an absolute error of approx. 0.5 μM is expected from the background subtraction (see Fig. S1† for details). (C) Average rate of hydrogen gas production during 1 h from anaerobic 2 mL *E. coli* cultures, concentrated from 100 mL batch cultures.

a comparison between background and H-cluster derived signals). For higher concentrations of $[2Fe]^{adt}$ in the cell medium (8–80 μM), the overall intensity of the EPR signal increased. Quantification of the signals *versus* a copper standard showed that a final total spin concentration of up to 10 μM was obtained following this protocol (Fig. 2B). However, the spectra became dominated by an axial signal originating from the CO inhibited state H_{ox}–CO ($g = 2.054$; 2.007).[48]

The successful assembly of functional enzyme was further verified by monitoring H_2 production from recombinant *E. coli* cells suspended in fresh M9 minimal medium. Hydrogen gas formation became clearly observable after the addition of 0.8 μM $[2Fe]^{adt}$ to the medium and increased up to 80 μM $[2Fe]^{adt}$, concomitantly with the overall EPR signal intensity (Fig. 2C). A maximum rate of 50–55 pmol H_2 per min per mL cell culture was observed, which corresponds to a specific activity of 10–15 nmol H_2 per min per mg assuming that the entire H-cluster population is detectable by EPR spectroscopy. The same titration trend was observed in *in vitro* assays. Hydrogenase activity assays performed on lysed cells demonstrated that a major fraction (approx. 80%) of the total available apo-HydA1 pool had formed the active $[2Fe]^{adt}$-HydA1 enzyme after 1 h incubation with 80 μM $[2Fe]^{adt}$ in the cell medium (Fig. S2†). Increasing the concentration of $[2Fe]^{adt}$ beyond this point resulted in a decline of *in vivo* H_2 production. Due to the dominance of H_{ox}–CO at higher $[2Fe]^{adt}$ concentration (Fig. 2B), the decreased H_2 productivity is attributed to release of CO from excess cofactor in the cell medium resulting in inhibition of the enzyme. The effect of the hydrogenase activity on the cytoplasmic pH was found to be negligible, with a decrease from pH 7.6 (±0.2) to 7.5 (±0.3) after incubation of the cells with $[2Fe]^{adt}$ for 60 minutes observed in separate assays using pH dependent fluorescent dyes. Consequently, a concentration of 80 μM $[2Fe]^{adt}$ in the cell medium was determined as optimal for the following mechanistic studies.

Investigating the integrity and enzymatic activity of single cells

The integrity and viability of the cells following anaerobic incubation in the presence of 80 μM $[2Fe]^{adt}$ was verified on batch level through a combination of SDS-PAGE, *in vitro* enzymatic assays, and plating experiments (Fig. S3 and S4†). Moreover, the integrity of individual cells was monitored by atomic force microscopy (AFM) on diluted *E. coli* samples (factor 5×10^{-5}). The topography suggested viable bacteria and only a limited number of cells were found to be morphologically altered (Fig. 3A and S5†). Subsequently, the local IR absorption of single cells was recorded using scattering-type scanning near-field optical microscopy (sSNOM). This label-free technique provides a chemical image of the cell at a spatial resolution of 30 nm.[49] To visualize the protein content in a number of representative cells, the amide I band ($\nu_1 = 1660$ cm^{-1}) was corrected for a topography feature at $\nu_2 = 1710$ cm^{-1} (Fig. 3A and Fig. S6† for additional examples). We found that the protein distribution was largely homogenous within the cells and no

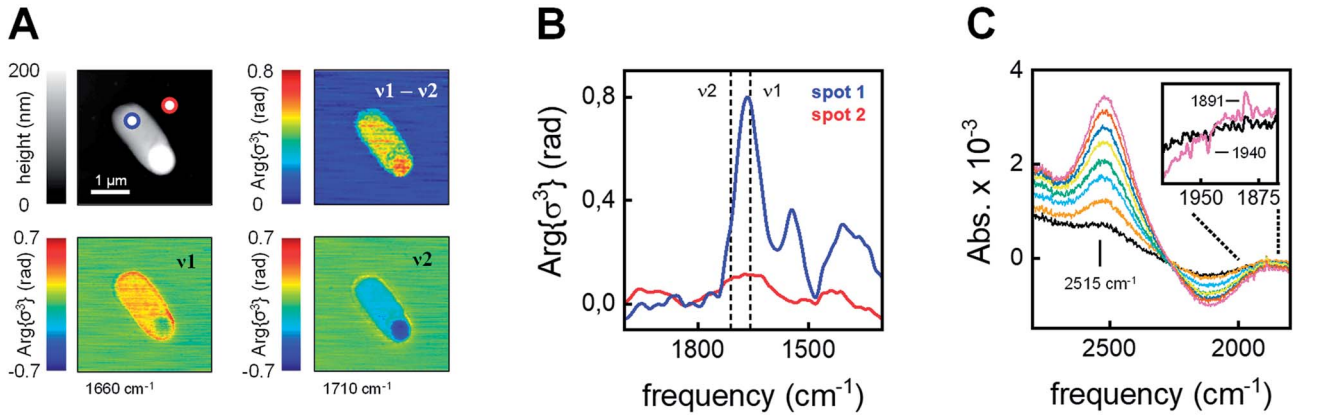

Fig. 3 Analysis of individual cells. (A) Upper left: AFM topography of a $[2Fe]^{adt}$–HydA1-containing *E. coli* cell. Lower left: sSNOM image mapped at $\nu_1 = 1660\ cm^{-1}$ (amide I absorption). Lower right: sSNOM image mapped at $\nu_2 = 1710\ cm^{-1}$ (topography artifact). Upper right: $\nu_1 - \nu_2$ sSNOM difference image. The protein is clearly localized to the cellular environment see Fig. S6 and S7† for additional examples. (B) Nano-FTIR near-field phase spectrum from 2000–1300 cm^{-1}. Spectra were recorded on the cell (spot 1, blue) and next to the cell (spot 2, red) in the AFM topography (panel A). (C) ATR FTIR difference spectra showed an HDO band (2515 cm^{-1}) increase in the presence of D_2 (exposure time 0–90 s increasing from black to purple). Inset: a simultaneous enrichment of H_{red} (1891 cm^{-1}) over H_{ox} (1940 cm^{-1}) was observed.

indication of secreted protein outside the cell was detected. Nano-FTIR near-field phase spectra showed typical amide I and amide II absorption within the cell, while such bands were not observed outside of the cell (Fig. 3B and S7† for additional examples). Moreover, only limited loss of H-cluster signal was observed upon washing *E. coli* cells in up to 10^8 time the volume of buffer (Fig. S8†). In combination with the aforementioned SDS-PAGE, *in vitro* enzymatic assays, and plating experiments (Fig. S3 and S4†), these findings underscore that our spectroscopy studies report on [FeFe]-hydrogenase located inside intact and viable cells.

In the next step, we used attenuated total reflection Fourier-transform infrared (ATR FTIR) spectroscopy to probe the catalytic competence of hydrated $[2Fe]^{adt}$-HydA1-containing *E. coli* films. Following reported protocols,[46] *E. coli* cell suspensions were deposited on the silicon crystal of the ATR optic, dried under inert gas (*i.e.*, N_2 or Ar), and rehydrated by running the gas through a wash bottle, forming a bacterial film that can react to changes in atmospheric gas composition. When the $[2Fe]^{adt}$-HydA1-containing *E. coli* film was kept under 100 mbar deuterium gas (D_2) instead of N_2, the appearance of a band at 2515 cm^{-1} suggests that deuterium ions (D^+) were released into bulk H_2O (Fig. 3C). This HDO band serves as direct verification of D_2 oxidation activity,[34] confirming that the [FeFe]-hydrogenase located inside the *E. coli* cells retained its activity in hydrated films. Additionally, H-cluster band shifts in the CO regime suggest reduction of H_{ox} into H_{red} (Fig. 3C, inset). Bacterial films containing apo-HydA1 did not show HDO formation under D_2 (Fig. S9†).

Mechanistic investigations on cell films using *in situ* ATR FTIR spectroscopy

The H-cluster-specific CO stretching vibrations in the frequency regime from 2050–1750 cm^{-1} were clearly resolved by ATR FTIR spectroscopy on $[2Fe]^{adt}$-HydA1-containing *E. coli* films. Under N_2, our data indicated predominantly oxidized enzyme with only minor contaminations of CO-inhibited cofactor (Fig. S9†). No trace of the free $[2Fe]^{adt}$ cofactor was detected. Exposing the film to 99% N_2 and 1% H_2 resulted in an enrichment of H_{red} over H_{ox} and H_{ox}–CO on a time-scale of seconds (Fig. 4A, spectrum a) whereas increasing the H_2 content to 100% had no further effects on the composition of redox states (Fig. S9†). Notably, neither H_{red}' nor H_{sred} were detected in $[2Fe]^{adt}$-HydA1-containing *E. coli* films (main CO marker bands at 1933 cm^{-1} and 1882 cm^{-1}, respectively). This is in contrast to purified $[2Fe]^{adt}$-HydA1 exposed to 100% H_2 and hints at specific differences (Fig. S10†). When the H_2 atmosphere was changed to N_2 again, the H-cluster converted quickly back into H_{ox} (Fig. 4A, spectrum b). The fact that H_{ox}–CO does not re-appear suggests a high degree of cofactor stability on the experimental time-scale (~10 min). When exposed to 1% CO, the oxidized H-cluster converted to H_{ox}–CO immediately (Fig. 4A, spectrum c).

Acidification of the $[2Fe]^{adt}$-HydA1-containing *E. coli* film *via* the aerosol (mixed buffer set to pH 4) and addition of 2 mM sodium dithionite (NaDT) caused a complete conversion of H_{ox} into $H_{ox}H$ within minutes (Fig. 4A, spectrum d and Fig. S10†).[23] The effect of this treatment on the cytoplasmic pH of $[2Fe]^{adt}$-HydA1 containing cells was determined in separate assays utilizing a commercial pH dependent fluorescent probe, as in the case of the H_2 producing cell suspensions. Incubation in pH 4 media resulted in a decrease from pH 7.5 (±0.3) to 6.1 (±0.1), however, the presence of up to 100 mM NaDT had negligible effect on the cytoplasmic pH both in pH 7.5 and 4 media. In the presence of H_2 or D_2, a quantitative enrichment of H_{hyd} over $H_{ox}H$ was observed (Fig. 4B, both spectra a). Increasing the NaDT concentration in the buffer to 100 mM enabled detection of H_{hyd} at pH 8 (Fig. S12†), suggesting that strongly reducing conditions allow the accumulation of this reactive intermediate already at weakly alkaline pH. Similar trends have been observed for the *in vitro* enrichment of $H_{ox}H$ and $H_{red}'H$.[23,26] Combining high NaDT concentrations and acidic pH resulted in the formation of a new species, shifted to higher frequencies

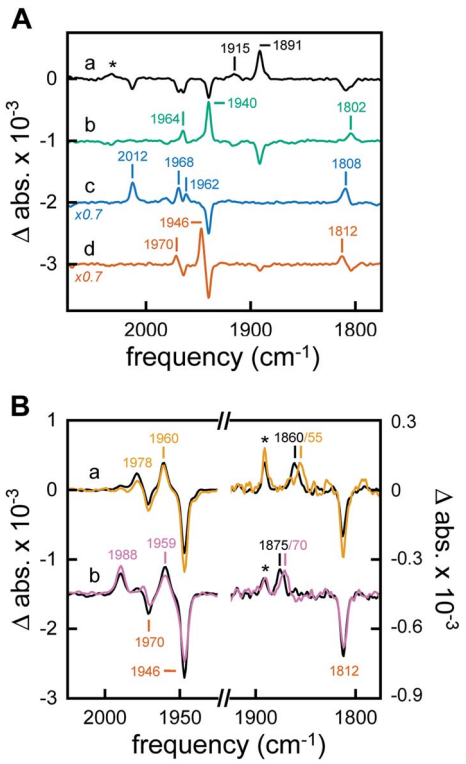

Fig. 4 ATR FTIR analysis of $[2Fe]^{adt}$-HydA1 containing *E. coli* cells. All difference spectra show the CO regime of the H-cluster. (A) In the presence of 1% H_2 (pH 8, 2 mM NaDT) freshly prepared cells converted from H_{ox} and H_{ox}–CO to H_{red} (spectrum a). * The band at 2032 cm^{-1} was attributed to a CN^- band of H_{red}. In the absence of H_2 quantitative enrichment of H_{ox} was observed (spectrum b). Exposure to 1% CO resulted in population of H_{ox}–CO (spectrum c). Under non-reducing, acidic conditions (N_2, pH 4, 2 mM NaDT) H_{ox} converted into $H_{ox}H$ (spectrum d). (B) In the presence of 1% H_2 (pH 4, 2 mM NaDT) formation of H_{hyd} over $H_{ox}H$ was observed (spectrum a, black line). Reduction with D_2 gas reproduced the hydride-specific downshift of the μCO band from 1860 to 1855 cm^{-1} (spectrum a, dark yellow line). Increasing the NaDT in the aerosol to 100 mM (pH 4, 1% H_2) facilitated accumulation of a new state, $H_{hyd}H^+$ (spectrum b, black line). The downshift of the μCO band under D_2 (1875 to 1870 cm^{-1}) verified the presence of a hydride ligand (spectrum b, purple line). * Small fraction of H_{red} at low pH.

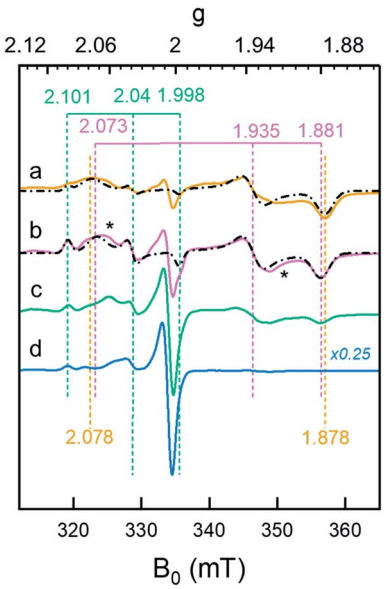

Fig. 5 Whole-cell generation of the H_{hyd} and $H_{hyd}H^+$ states under different conditions probed by EPR spectroscopy. (a) The H_{hyd} state was observable in EPR spectra recorded on $[2Fe]^{adt}$-HydA1 containing cells at pH 7.5, complemented with 10 mM NaDT, flushed with H_2 for 15 min and rapidly frozen (dark yellow spectrum); (b): A new signal attributed to $H_{hyd}H^+$ was observed in samples prepared as lane a but at pH 4 (purple spectrum); (c) samples prepared as lane b but excluding NaDT generated a weaker $H_{hyd}H^+$ signal (green spectrum); (d) samples prepared as lane b but excluding H_2 flushing did not generate any discernable $H_{hyd}H^+$ signal (blue spectrum). The *g*-values of $H_{ox}/H_{ox}H$ (green dashed vertical lines), H_{hyd} (dark yellow dashed vertical lines) and $H_{hyd}H^+$ (purple dashed vertical lines) states are based on the simulations of the spectra (black dash-dotted lines), for details see Fig. S13.† Unassigned weak signals potentially arising from an H_{trans}-like state indicated with asterisks.[40] EPR experimental conditions: T = 20 K, P = 1 mW, ν = 9.38 GHz.

by up to 15 cm^{-1} as compared to the previously reported H_{hyd} state (Fig. 4B, both spectra b). Reference experiments on purified $[2Fe]^{adt}$-HydA1 in the presence of pH 4, 100 mM NaDT, and 1% H_2 confirmed the possibility of generating this species *in vitro*. Additionally, it facilitated a precise assignment of the CO/CN^- band positions (Fig. S12†). To verify that this new signal reflected a hydride-binding form of the H-cluster, the same species was generated using D_2, which resulted in the expected downshift of the bridging carbonyl band[40] from 1875 to 1870 cm^{-1} (Fig. 4B, purple spectrum b).

Making use of *in situ* ATR FTIR spectroscopy on $[2Fe]^{adt}$-HydA1-containing *E. coli* cells, we were able to observe several H-cluster states previously identified on purified hydrogenase. It is worth noting that H_{sred} and H_{red}' were never observed under whole-cell conditions. The accumulation of H_{red}' depends on intermolecular electron transfer and the concentration of enzyme,[23] which explains the lack of signal in Fig. 4A. Fig. S11† demonstrates that no such correlation was observed for H_{sred}, providing indirect support for the notion that our data report exclusively on $[2Fe]^{adt}$-HydA1 within *E. coli* cells. Conversely, H_{hyd} and the new hydride-like state readily accumulated under acidic conditions and could be selectively enriched as a function of NaDT concentration. A similar hydride-like state was reported earlier[34,40] but has not been characterized in detail. Compared to H_{hyd}, the observed spectral up-shifts are larger and less consistent than those previously attributed to protonation changes at the $[4Fe–4S]_H$ cluster, *e.g.* in $H_{ox}H$ (Fig. S12†).[23,26] DFT calculations carried out by Mulder *et al.* have attributed shifts of similar magnitude to protonation changes at the $[2Fe]_H$ subsite.[40] Thus, we assign this species to a new hydride state featuring a nitrogen-protonated azadithiolate ligand, $H_{hyd}H^+$.

Two different hydride-like states observed by EPR as a function of pH

The formation of H_{hyd}, as well as an alternative hydride-like state formed at low pH, was corroborated by EPR spectroscopy. A rhombic signal (g_{zyx} = 2.078, 1.935, 1.878) in good

agreement with the *in vitro* identified H_{hyd} state was observed for weakly alkaline $[2Fe]^{adt}$-HydA1 containing *E. coli* suspensions, rapidly frozen after incubation with NaDT and H_2 (Fig. 5, spectrum a and Fig. S13, Table S3†).[35,39,40] The g_y and g_x positions of this H_{hyd} signal were readily apparent in spectra recorded at both 10 and 20 K (Fig. S14,† orange spectra), while the broad nature of the feature observed at $g \approx 2.08$–2.07 complicated an exact assignment of the g_z position. Spectra recorded at higher microwave power ($P \geq 8$ mW) simplified the low-field region and were consequently used for the g_z assignment (Fig. S15†). Small contributions from H_{ox} were still visible in the spectrum, in combination with an additional minor rhombic signal (Fig. 5 and S13†). Conversely, including an H_{ox}–CO component in the simulation did not improve the overall fit. Thus, the central $g \approx 2.0$ feature is most likely attributable to EPR active species native to *E. coli*. Finally, it is noteworthy that the H_{hyd} signal was readily observable in cells incubated under an H_2 atmosphere even in the absence of NaDT, supporting its physiological relevance.

A new rhombic H_{hyd}-like signal was observed when the analogous experiment was performed in media acidified to pH 4 (Fig. 5, spectrum b and S13–S15†). As the signal accumulates under conditions similar to those of $H_{hyd}H^+$ in ATR FTIR, we assign this signal to the same protonated hydride state. Similar to the H_{hyd} signal, the low pH rhombic signal saturates by only 30% at 100 mW ($T = 20$ K), illustrating fast spin relaxation of the center (Fig. S15†). An exact assignment of the g_z position was challenging also for $H_{hyd}H^+$, due to the complex nature of the g_z region at low microwave powers (Fig. S13–S15†). Still, in comparison to H_{hyd} the $H_{hyd}H^+$ spectrum featured a clearly discernible decreased anisotropy ($g_{zyx} = 2.073, 1.935, 1.881$, vertical purple dashed lines in Fig. 5), and the g_z component became more distinct at higher microwave power ($P \geq 8$mW, see Fig. S15†). We assign the observed shift of the H_{ox} g_z position from 2.100 to 2.101 at low pH to the formation of $H_{ox}H$. Attempts at simulating the high pH H_{hyd} spectrum as a combination of $H_{hyd}H^+$ and H_{sred} did not yield reasonable results, further supporting that these three rhombic EPR signals arise from different states (Table S3†). Based on the similarity of the rhombic $H_{hyd}H^+$ signal to that observed for the H_{hyd} state in particular,[40] but also the H_{trans} state,[21] it is attributed to a species featuring a reduced $[4Fe–4S]_H$ cluster coupled to a diamagnetic $[Fe(II)Fe(II)]_H$ subsite, closely resembling the H_{hyd} state.

Exposing apo-HydA1 containing cells to H_2 in the presence or absence of NaDT did not result in any spectral features similar to $H_{hyd}H^+$, neither did BL21(DE3) *E. coli* cells lacking the *hyda1* gene. The transient nature of the $H_{hyd}H^+$ state in cell suspensions was verified by exchanging the H_2 atmosphere with Ar for 30 minutes, which resulted in a loss of $H_{hyd}H^+$ and conversion back to a mixture of oxidized states (H_{ox} and H_{ox}–CO). Interestingly, the presence of NaDT in the cell medium during H_2 treatment was not strictly required for the generation of the $H_{hyd}H^+$ state (Fig. 5, compare spectra a and c). Increasing the NaDT concentration in the cell suspension up to 100 mM, *i.e.* conditions shown to favor accumulation of the $H_{hyd}H^+$ state under ATR FTIR conditions (Fig. 4B), resulted in a more intense $H_{hyd}H^+$ signal but no distinct new spectral features were observed. Conversely, no $H_{hyd}H^+$ signal was discernible in the absence of H_2, irrespective of NaDT concentration (Fig. 5, spectrum d).

Conclusions

The artificial maturation of apo-HydA1 in *E. coli* provides access to high concentrations of [FeFe]-hydrogenase *in vivo*. Furthermore, cellular H_2 oxidation and production verify that the resulting semi-synthetic HydA1 enzyme is functional and connects to the cell metabolism, most likely *via* ferredoxins.[6] This has facilitated the first mechanistic investigation of an [FeFe]-hydrogenase under whole-cell conditions, employing EPR and FTIR spectroscopy as complementary techniques. Despite differences in sample preparation and experimental conditions (*i.e.* cell suspension *vs.* cell film, cryogenic *vs.* ambient temperatures) both techniques reveal the same trends.

The dominant oxidation states under weakly alkaline conditions are H_{ox} and H_{ox}–CO. In addition, FTIR spectroscopy on hydrated films showed that H_{red} was enriched in the presence of H_2. This transition was rapid and quantitative but the enzyme converted back to H_{ox} when H_2 was removed from the gas phase. Similar reactivity ("auto-oxidation") is generally observed for HydA1 *in vitro* and is clearly retained *in vivo*. It is noteworthy that diverging reactivity was recently reported for two putative sensory [FeFe]-hydrogenases of different origin, which appear to stabilize in an H_{red}-like state both *in vitro* and in whole cells.[46,50] This arguably reflects the different physiological roles of sensory hydrogenases and the prototypical HydA1 enzyme.[51]

In addition to the relatively stable catalytic intermediates H_{ox} and H_{red}, the study revealed complex metal-hydride chemistry occurring in living cells and two different hydride states were observed. The EPR spectra recorded on cell suspensions incubated under a neat H_2 atmosphere in weakly alkaline buffer revealed the formation of the H_{hyd} state. This finding verifies that this proposed catalytic intermediate is generated under physiologically relevant conditions, *i.e.* in the absence of the artificial reductant dithionite and in weakly alkaline cell medium where the cytoplasmic pH is ≈7.5. The whole-cell formation of H_{hyd} was also confirmed by FTIR spectroscopy. Acidification of the cell medium resulted in decrease of cytoplasmic pH and rapid formation of $H_{ox}H$. Exposing the acidified cells to reducing conditions resulted in accumulation of H_{hyd}, previously only observed *in vitro*. Moreover, the complementary nature of EPR and FTIR spectroscopy has allowed us to detect and characterize an additional hydride-like state, denoted $H_{hyd}H^+$. The existence of alternative hydride-like states have been suggested earlier from work on HydA1, often in amino acid variants with impaired proton transfer capacity, but has so far been challenging to accumulate and consequently not characterized in detail.[32–35,37,40] Herein, we show how such an alternative hydride-like state, $H_{hyd}H^+$, can be selectively generated also in the fully functional enzyme, not only *in vitro* but also under whole-cell conditions. The assignment of $H_{hyd}H^+$ as a hydride state is confirmed by the observed H/D isotopic shift of the μ-CO ligand. The pH

dependence and spectral up-shift relative to H_{hyd}, as well as earlier DFT calculations, supports that this hydride state features a protonated nitrogen bridgehead atom.[40] Additionally, the relatively small change observed in the corresponding EPR spectra supports a model in which the electronic configuration of H_{hyd} remains unchanged (*i.e.* $[4Fe–4S]_H^+$-$[Fe(II)Fe(II)]_H$) upon protonation, as the latter technique reports primarily on the paramagnetic $[4Fe–4S]_H^+$ cluster. The relatively facile accumulation of this species is somewhat surprising, as it should readily proceed to produce H_2. However, it is likely a result of the relatively flat energy landscape of H^+/H_2 interconversion necessary for the remarkable catalytic efficiency of the enzyme, which has already enabled the stabilization of a wide range of potential catalytic intermediates through gas, pH and redox potential manipulations. The possibility to accumulate the $H_{hyd}H^+$ state also *in vitro* should enable in-depth studies, providing more detailed insight into its structure. Moreover, having elucidated its FTIR fingerprint will allow probing for it in transient spectroscopy to verify its catalytic competence.

In conclusion, the expansion of artificial maturation to *in vivo* conditions in combination with our capacity to manipulate and spectroscopically investigate [FeFe]-hydrogenases in whole cells has allowed us to support the physiological relevance of a number of proposed catalytic intermediates. In the context of mechanistic understanding, $H_{hyd}H^+$ potentially represent the last isolatable intermediate in the transition from H_{hyd} to H_{ox} with concomitant H_2 formation. Deciphering and mapping out the reactivity of this hydride species represents an exciting future prospect, expected to provide critical insight into H_2 formation and cleavage.

Experimental

General

All chemicals were purchased from Sigma-Aldrich or VWR and used as received unless otherwise stated. All anaerobic work was performed in an MBRAUN glovebox ($[O_2]$ < 10 ppm). The expression vector encoding the *hydA1* gene (pETDuet-CrHydA1-His) was kindly provided by Prof. Marc Fontecave (Collège de France, Paris/CEA, Grenoble). $(Et_4N)_2[Fe_2(adt)(CO)_4(CN)_2]$ ($[2Fe]^{adt}$) was synthesized in accordance to literature protocols with minor modifications, and verified by FTIR spectroscopy.[52–55] The complex was dissolved in anaerobic potassium phosphate buffer (100 mM, pH 6.8) at 10 ng μL^{-1} to 10 $\mu g\ \mu L^{-1}$ concentration and used directly. Protein content was analyzed by 10% SDS-PAGE minigels in a BioRad Mini-PROTEAN Tetra Cell system. The proteins were stained with Page Blue protein staining solution (Thermo Fisher Scientific) according to the supplier's instructions.

Overexpression of the apo-HydA1 hydrogenase

Escherichia coli BL21(DE3) cells containing the HydA1 plasmid were grown in 50 mL M9 medium [22 mM Na_2HPO_4, 22 mM KH_2PO_4, 85 mM NaCl, 18 mM NH_4Cl, 0.2 mM $MgSO_4$, 0.1 mM $CaCl_2$, 0.4% (v/v) glucose] under aerobic conditions until $O.D._{600}$ = 0.6–0.8 in the presence of ampicillin. The protein overproduction was induced with 1 mM IPTG and persisted at 20 °C for 16–18 h with continuous aeration. The media was supplemented with 100 μM $FeSO_4$ at the time of the induction. Final $O.D._{600}$ of the cultures were 1.4 ± 0.2.

In vivo formation of $[2Fe]^{adt}$-HydA1

The preparation of the semi-synthetic hydrogenase was performed following a literature protocol with minor modifications.[44,45] The apo-HydA1 protein was expressed in 50 mL *E. coli* cultures as described in the "*Overexpression of the apo-HydA1 hydrogenase*" section. After the 16–18 h expression period the cells were harvested, deaerated and transferred to the glove-box. The cells were re-suspended in fresh M9 medium (2 mL final volume), and formation of $[2Fe]^{adt}$–HydA1 was achieved by treating the cell suspensions with 100 μg (156 nmol) $[2Fe]^{adt}$ complex (80 mM final conc.), unless otherwise stated, for 1 h at 37 °C under strictly anaerobic conditions.

Whole-cell EPR and FTIR sample preparation

The 2 mL concentrated cell suspensions generated *via* the "*In vivo formation of* $[2Fe]^{adt}$*-HydA1*" protocol were centrifuged and the cell pellet washed with 1 mL Tris–HCl buffer (100 mM Tris, 150 mM NaCl pH 7.5) three times under anaerobic conditions. For EPR samples the cells were diluted to a final volume of 400 μL with Tris–HCl buffer after the washing protocol and transferred into EPR tubes. The tubes were capped and directly frozen in liquid nitrogen. In case of FTIR samples four separate 2 mL sample preparations were combined, concentrated and diluted to 400 μL with Tris–HCl buffer and frozen in liquid nitrogen under anaerobic conditions.

Generation of the H_{hyd} EPR samples

The apo-HydA1 containing cells were activated as described above. After activation the cells were washed with Tris–HCl buffer (100mM Tris, 150mM NaCl) and re-suspended 400 μL buffer under anaerobic conditions. When indicated, the Tris–HCl buffer was complemented with 10 or 100 mM Na-dithionite. The H_2 treated samples were flushed with H_2 gas for 15 min under anaerobic conditions. After flushing the cells were quickly transferred into EPR tubes. The tubes were capped and flash frozen in liquid nitrogen. The pH of the Tris–HCl buffer was either pH 7.5 or pH 4 according to the experiment, and verified before and after each flushing experiment. Plating the cells on ampicillin enriched LB-agar plates as well as SDS-PAGE gel analysis and *in vitro* enzymatic assays were used to ensure the viability and integrity of the cells also under low pH conditions (Fig. S3†).

Hydrogenase activity measurements

In vivo and *in vitro* activity measurements were performed according to published protocols.[44] Hydrogen production was determined by analyzing the head-space gas, using a gas chromatograph (GC; PerkinElmer LLC, MA, USA) equipped with a thermal conductivity detector (TCD) and a stainless-steel column packed with Molecular Sieve (60/80 mesh). A

calibration curve was established by injecting known amounts of hydrogen. The operational temperatures of the injection port, the oven and the detector were 100 °C, 80 °C and 100 °C, respectively. Argon was used as the carrier gas at a flow rate of 35 mL min^{-1}.

EPR measurements

The EPR spectra shown are representative signals from at least two individual experiments. The individual experiments show some preparation dependent differences, but the amplitude of these background signals are negligible compared to the signal intensity of the $[2Fe]^{adt}$ activated HydA1. Measurements were performed on a Bruker ELEXYS E500 spectrometer using an ER049X SuperX microwave bridge in a Bruker SHQ0601 cavity (Fig. 2) or a Bruker EMX micro equipped with an EMX Premium bridge and an ER4119 HS resonator (Fig. 5 and S13–S15†), both equipped with an Oxford Instruments continuous flow cryostat and using an ITC 503 temperature controller (Oxford Instruments). Measurement temperatures ranged from 10 to 20 K, using liquid helium as coolant, with the following EPR settings unless otherwise stated: microwave power 1 mW, modulation amplitude 1 mT, modulation frequency 100 kHz. The spectrometer was controlled by the Xepr software package (Bruker).

EPR spectra processing, simulations and spin quantification

The EPR spectra were processed using the softwares Matlab (Mathworks, Inc) and QSoas.[56] Matlab served for converting the EPR files to ascii format, while QSoas was used to display the spectra as a function of g values, for visual inspection and subtraction of background signals emerging from the cells. The processed signals were used for Fig. 2, 5 and S13.† The simulations were performed using the easyspin toolbox (5.2.23) within Matlab.[57] The positions and line-width of each signature were manually adjusted to fit the experimental features, and kept the same across all datasets. Other details of the procedure can be found in ref. 45.

Infrared measurements

For whole-cell ATR FTIR spectroscopy, 1 μL *E. coli* suspension was deposited on the silicon crystal of an ATR cell in the beam path of a commercial FTIR spectrometer (Bruker). All experiments were performed at ambient temperature (~24 °C) and pressure (~1 atm), in the dark, and on hydrated films. The cell suspension was dried under 100% N_2 gas and re-hydrated with buffer solution (100 mM Tris, MES, and PIPPS) in the humidified gas stream (aerosol), similar to what was reported for purified protein earlier.[23] The utilized buffer mix allowed titrating the cell film between pH 9 and pH 4. Reduction of [FeFe]-hydrogenase in the cells was induced by adding 1–100% H_2 to the N_2 gas stream (flow volume 1.5 L min^{-1}). In the absence of H_2 (100% N_2), the oxidized resting state (H_{ox} or $H_{ox}H$) recovered due to auto-oxidation. Plating experiments were performed to verify cell viability after the FTIR experiments (Fig. S4†) Transitions were followed with a spectral precision of 2 cm^{-1} and 1000 averages of interferometer scans per spectrum. Difference spectra were calculated by subtraction of single absorbance spectra recorded under varying conditions (*e.g.*, H_2 – N_2, pH 4 – pH 8, *etc.*)

Single cell analysis

For single-cell AFM, sSNOM and nano-FTIR cell suspensions were diluted by a factor of 5×10^5 (1 : 20 000) and a 1 μL droplet was dried on template stripped gold substrate. Topographies, near-field maps and spectra were acquired under ambient conditions. For other technical details, the setup is described in the ESI Section, Fig. S16.†

Cytoplasmic pH quantification

The intracellular pH of the pH 4 and pH 7.5 incubated cells were quantified with pH Rhodo™ Green AM Intracellular pH Indicator in combination with the Intracellular pH Calibration Buffer Kit (Thermo Fisher Scientific). This method determines intracellular pH using the pHrodo™ Red fluorescent dye and is applicable to a range of cell types.[58,59] Modification of pHrodo™ Red and Green dyes with acetomyxethyl (AM) ester groups results in an uncharged molecule that can permeate cell membranes. Once inside the cell, the lipophilic blocking groups are cleaved by nonspecific esterases, resulting in a compound that is retained within the intracellular space.

More specifically, 50 mL cultures of *E.coli* cells containing the overproduced apo-HydA1 protein were concentrated down to 2 mL and parallel vials were either treated with 80 μM $[2Fe]^{adt}$ or left untreated for 1 h, before the cell suspensions were centrifuged and washed three times in 1 mL pH 7.5 or pH 4 Tris–HCl media respectively. After washing, the cells were further incubated in 1 mL pH 4 or pH 7.5 Tris -HCl media with or without 100 mM Na-dithionite for 30 minutes under anaerobic conditions. After removal of the incubation buffer through centrifugation, the cells were re-suspended in 500 uL Live Cell Imaging Solution (Thermo Scientific) containing 10 μL Rodo Green dye. 100 μL of the resulting solutions were pipetted into a 96-well microplate. Every experimental condition was measured in four parallels. The fluorescent signals were detected using a Hidex Chameleon plate reader with 495 nm excitation and 590 nm emission filters. The intercellular pH in the different samples were calculated using the calibration curve obtained using the Intracellular pH Calibration Buffer Kit (Thermo Sceintific). For the latter, 50 mL cultures of *E.coli* cells containing the overproduced apo-HydA1 were centrifuged and washed three times in 1 mL pH 7.5 Tris–HCl buffer. After washing, the cells were suspended in 500 μL Intracellular pH Calibration Buffer, component A, B, C or D (Thermo Scientific, covering a pH range of 4.5–7.5) containing 10 μM valinomicin/ 10 μM nigericin (Thermo Scientific).

Conflicts of interest

There are no conflicting interests to declare.

Acknowledgements

We thank Dr. Basem Soboh for support with the plating experiments and Dr. Ping Huang for discussions concerning EPR spectra analysis. The European Research Council (GB, StG contract no. 714102) and the Olle Engkvist Byggmästare foundation (GB and LM) are gratefully acknowledged for funding. The Deutsche Forschungsgemeinschaft (DFG) is acknowledged for financial support to STS (STR 1554/5-1) and JH (HE 2063/5-1). Part of the project is funded by the DFG under Germany's Excellence Strategy – EXC 2008/1-390540038 (UniSysCat) to JH. The European Union's Horizon 2020 research and innovation programme is gratefully acknowledged for funding to MS (under the Marie Skłodowska-Curie grant agreement No. 897555).

Notes and references

1 C. Madden, M. D. Vaughn, I. Díez-Pérez, K. A. Brown, P. W. King, D. Gust, A. L. Moore and T. A. Moore, *J. Am. Chem. Soc.*, 2012, **134**, 1577–1582.
2 W. Lubitz, H. Ogata, O. Rüdiger and E. Reijerse, *Chem. Rev.*, 2014, **114**, 4081–4148.
3 M. Hambourger, M. Gervaldo, D. Svedruzic, P. W. King, D. Gust, M. Ghirardi, A. L. Moore and T. A. Moore, *J. Am. Chem. Soc.*, 2008, **130**, 2015–2022.
4 S. Krishnan and F. A. Armstrong, *Chem. Sci.*, 2012, **3**, 1015–1023.
5 N. Plumeré, O. Rüdiger, A. A. Oughli, R. Williams, J. Vivekananthan, S. Pöller, W. Schuhmann and W. Lubitz, *Nat. Chem.*, 2014, **6**, 822–827.
6 A. Wegelius, N. Khanna, C. Esmieu, G. D. Barone, F. Pinto, P. Tamagnini, G. Berggren and P. Lindblad, *Energy Environ. Sci.*, 2018, **11**, 3163–3167.
7 C. Esmieu, P. Raleiras and G. Berggren, *Sustainable Energy Fuels*, 2018, **2**, 724–750.
8 T. R. Simmons, G. Berggren, M. Bacchi, M. Fontecave and V. Artero, *Coord. Chem. Rev.*, 2014, **270–271**, 127–150.
9 C. Tard and C. J. Pickett, *Chem. Rev.*, 2009, **109**, 2245–2274.
10 M. Haumann and S. T. Stripp, *Acc. Chem. Res.*, 2018, **51**, 1755–1763.
11 B. L. Greene, G. J. Schut, M. W. W. Adams and R. B. Dyer, *ACS Catal.*, 2017, **7**, 2145–2150.
12 J. W. Peters, W. N. Lanzilotta, B. J. Lemon and L. C. Seefeldt, *Science*, 1998, **282**, 1853–1858.
13 G. Berggren, A. Adamska, C. Lambertz, T. R. Simmons, J. Esselborn, M. Atta, S. Gambarelli, J. M. Mouesca, E. Reijerse, W. Lubitz, T. Happe, V. Artero and M. Fontecave, *Nature*, 2013, **499**, 66–69.
14 A. Silakov, B. Wenk, E. Reijerse and W. Lubitz, *Phys. Chem. Chem. Phys.*, 2009, **11**, 6592–6599.
15 Y. Nicolet, C. Piras, P. Legrand, C. E. Hatchikian and J. C. Fontecilla-Camps, *Structure*, 1999, **7**, 13–23.
16 M. C. Posewitz, P. W. King, S. L. Smolinski, L. Zhang, M. Seibert and M. L. Ghirardi, *J. Biol. Chem.*, 2004, **279**, 25711–25720.
17 P. W. King, M. C. Posewitz, M. L. Ghirardi and M. Seibert, *J. Bacteriol.*, 2006, **188**, 2163–2172.
18 E. M. Shepard, F. Mus, J. N. Betz, A. S. Byer, B. R. Duffus, J. W. Peters and J. B. Broderick, *Biochemistry*, 2014, **53**, 4090–4104.
19 G. Caserta, L. Pecqueur, A. Adamska-Venkatesh, C. Papini, S. Roy, V. Artero, M. Atta, E. Reijerse, W. Lubitz and M. Fontecave, *Nat. Chem. Biol.*, 2017, **13**, 779–784.
20 G. Rao, L. Tao, D. L. M. Suess and R. D. Britt, *Nat. Chem.*, 2018, **10**, 555–560.
21 S. P. J. Albracht, W. Roseboom and E. C. Hatchikian, *J. Biol. Inorg Chem.*, 2006, **11**, 88–101.
22 A. Silakov, E. J. Reijerse, S. P. J. Albracht, E. C. Hatchikian and W. Lubitz, *J. Am. Chem. Soc.*, 2007, **129**, 11447–11458.
23 M. Senger, S. Mebs, J. Duan, O. Shulenina, K. Laun, L. Kertess, F. Wittkamp, U.-P. Apfel, T. Happe, M. Winkler, M. Haumann and S. T. Stripp, *Phys. Chem. Chem. Phys.*, 2018, **20**, 3128–3140.
24 B. Bennett, B. J. Lemon and J. W. Peters, *Biochemistry*, 2000, **39**, 7455–7460.
25 S. Katz, J. Noth, M. Horch, H. S. Shafaat, T. Happe, P. Hildebrandt and I. Zebger, *Chem. Sci.*, 2016, **7**, 6746–6752.
26 M. Senger, K. Laun, F. Wittkamp, J. Duan, M. Haumann, T. Happe, M. Winkler, U.-P. Apfel and S. T. Stripp, *Angew. Chem., Int. Ed.*, 2017, **56**, 16503–16506.
27 C. Sommer, A. Adamska-Venkatesh, K. Pawlak, J. A. Birrell, O. Rüdiger, E. J. Reijerse and W. Lubitz, *J. Am. Chem. Soc.*, 2017, **139**, 1440–1443.
28 A. Adamska, A. Silakov, C. Lambertz, O. Rüdiger, T. Happe, E. Reijerse and W. Lubitz, *Angew. Chem., Int. Ed.*, 2012, **51**, 11458–11462.
29 E. J. Reijerse, C. C. Pham, V. Pelmenschikov, R. Gilbert-Wilson, A. Adamska-Venkatesh, J. F. Siebel, L. B. Gee, Y. Yoda, K. Tamasaku, W. Lubitz, T. B. Rauchfuss and S. P. Cramer, *J. Am. Chem. Soc.*, 2017, **139**, 4306–4309.
30 M. W. Ratzloff, J. H. Artz, D. W. Mulder, R. T. Collins, T. E. Furtak and P. W. King, *J. Am. Chem. Soc.*, 2018, **140**, 7623–7628.
31 M. L. K. Sanchez, C.-H. Wu, M. W. W. Adams and R. B. Dyer, *Chem. Commun.*, 2019, **55**, 5579–5582.
32 J. A. Birrell, V. Pelmenschikov, N. Mishra, H. Wang, Y. Yoda, K. Tamasaku, T. B. Rauchfuss, S. P. Cramer, W. Lubitz and S. DeBeer, *J. Am. Chem. Soc.*, 2020, **142**, 222–232.
33 C. Lorent, S. Katz, J. Duan, C. J. Kulka, G. Caserta, C. Teutloff, S. Yadav, U.-P. Apfel, M. Winkler, T. Happe, M. Horch and I. Zebger, *J. Am. Chem. Soc.*, 2020, **142**, 5493–5497.
34 M. Winkler, M. Senger, J. Duan, J. Esselborn, F. Wittkamp, E. Hofmann, U.-P. Apfel, S. T. Stripp and T. Happe, *Nat. Comm.*, 2017, **8**, 16115.
35 D. W. Mulder, Y. Guo, M. W. Ratzloff and P. W. King, *J. Am. Chem. Soc.*, 2017, **139**, 83–86.
36 S. Rumpel, C. Sommer, E. Reijerse, C. Farès and W. Lubitz, *J. Am. Chem. Soc.*, 2018, **140**, 3863–3866.
37 V. Pelmenschikov, J. A. Birrell, C. C. Pham, N. Mishra, H. Wang, C. Sommer, E. Reijerse, C. P. Richers, K. Tamasaku, Y. Yoda, T. B. Rauchfuss, W. Lubitz and S. P. Cramer, *J. Am. Chem. Soc.*, 2017, **139**, 16894–16902.

38 C. C. Pham, D. W. Mulder, V. Pelmenschikov, P. W. King, M. W. Ratzloff, H. Wang, N. Mishra, E. E. Alp, J. Zhao, M. Y. Hu, K. Tamasaku, Y. Yoda and S. P. Cramer, *Angew. Chem., Int. Ed.*, 2018, **57**, 10605–10609.
39 D. W. Mulder, M. W. Ratzloff, E. M. Shepard, A. S. Byer, S. M. Noone, J. W. Peters, J. B. Broderick and P. W. King, *J. Am. Chem. Soc.*, 2013, **135**, 6921–6929.
40 D. W. Mulder, M. W. Ratzloff, M. Bruschi, C. Greco, E. Koonce, J. W. Peters and P. W. King, *J. Am. Chem. Soc.*, 2014, **136**, 15394–15402.
41 J. Esselborn, C. Lambertz, A. Adamska-Venkatesh, T. Simmons, G. Berggren, J. Noth, J. Siebel, A. Hemschemeier, V. Artero, E. Reijerse, M. Fontecave, W. Lubitz and T. Happe, *Nat. Chem. Biol.*, 2013, **9**, 607–609.
42 J. F. Siebel, A. Adamska-Venkatesh, K. Weber, S. Rumpel, E. Reijerse and W. Lubitz, *Biochemistry*, 2015, **54**, 1474–1483.
43 J. A. Birrell, O. Rüdiger, E. J. Reijerse and W. Lubitz, *Joule*, 2017, **1**, 61–76.
44 N. Khanna, C. Esmieu, L. S. Meszaros, P. Lindblad and G. Berggren, *Energy Environ. Sci.*, 2017, **10**, 1563–1567.
45 L. S. Mészáros, B. Németh, C. Esmieu, P. Ceccaldi and G. Berggren, *Angew. Chem., Int. Ed.*, 2018, **57**, 2596–2599.
46 H. Land, P. Ceccaldi, L. S. Mészáros, M. Lorenzi, H. J. Redman, M. Senger, S. T. Stripp and G. Berggren, *Chem. Sci.*, 2019, **10**, 9941–9948.
47 S. T. Stripp and T. Happe, *Dalton Trans.*, 2009, 9960–9969, DOI: 10.1039/b916246a.
48 C. Kamp, A. Silakov, M. Winkler, E. J. Reijerse, W. Lubitz and T. Happe, *Biochim. Biophys. Acta, Bioenerg.*, 2008, **1777**, 410–416.
49 I. Amenabar, S. Poly, W. Nuansing, E. H. Hubrich, A. A. Govyadinov, F. Huth, R. Krutokhvostov, L. Zhang, M. Knez, J. Heberle, A. M. Bittner and R. Hillenbrand, *Nat. Comm.*, 2013, **4**, 2890.
50 N. Chongdar, J. A. Birrell, K. Pawlak, C. Sommer, E. J. Reijerse, O. Rüdiger, W. Lubitz and H. Ogata, *J. Am. Chem. Soc.*, 2018, **140**, 1057–1068.
51 C. Greening, A. Biswas, C. R. Carere, C. J. Jackson, M. C. Taylor, M. B. Stott, G. M. Cook and S. E. Morales, *ISME J.*, 2015, **10**, 761.
52 A. Le Cloirec, S. C. Davies, D. J. Evans, D. L. Hughes, C. J. Pickett, S. P. Best and S. Borg, *Chem. Commun.*, 1999, 2285–2286.
53 E. J. Lyon, I. P. Georgakaki, J. H. Reibenspies and M. Y. Darensbourg, *Angew. Chem., Int. Ed.*, 1999, **38**, 3178–3180.
54 M. Schmidt, S. M. Contakes and T. B. Rauchfuss, *J. Am. Chem. Soc.*, 1999, **121**, 9736–9737.
55 H. Li and T. B. Rauchfuss, *J. Am. Chem. Soc.*, 2002, **124**, 726–727.
56 V. Fourmond, *Anal. Chem.*, 2016, **88**, 5050–5052.
57 S. Stoll and A. Schweiger, *J. Magn. Reson.*, 2006, **178**, 42–55.
58 M. Ogawa, N. Kosaka, C. A. Regino, M. Mitsunaga, P. L. Choyke and H. Kobayashi, *Mol. BioSyst.*, 2010, **6**, 888–893.
59 L. V. Deriy, E. A. Gomez, G. Zhang, D. W. Beacham, J. A. Hopson, A. J. Gallan, P. D. Shevchenko, V. P. Bindokas and D. J. Nelson, *J. Biol. Chem.*, 2009, **284**, 35926–35938.